

## Article

# A Thermal Model to Estimate PV Electrical Power and Temperature Profile along Panel Thickness

Francesco Nicoletti <sup>1,\*</sup> , Mario Antonio Cucumo <sup>1</sup>, Vittorio Ferraro <sup>2</sup>, Dimitrios Kaliakatsos <sup>1</sup>   
and Albino Gigliotti <sup>1</sup> 

<sup>1</sup> Mechanical, Energy and Management Engineering Department, University of Calabria, 87036 Rende, Italy

<sup>2</sup> Computer, Modelling, Electronics and System Engineering Department, University of Calabria, 87036 Rende, Italy

\* Correspondence: francesco.nicoletti@unical.it

**Abstract:** The production of electricity from photovoltaic panels has experienced significant developments. To manage the energy flows introduced into the electricity grid, it is necessary to estimate the productivity of PV panels under the climatic conditions. In this study, a photovoltaic panel is modelled from thermal and electrical points of view to evaluate electrical performance and identify the temperature distribution in the layers. The analysis performed is time dependent and the problem is solved using the finite difference technique. A methodology is introduced to estimate the cloudiness of the sky, which affects radiative heat exchange. The calculation method is validated using experimental data recorded in a laboratory of the University of Calabria. Temperature and electrical power are predicted with RMSE of 1.5–2.0 °C and NRMSE of 1.2–2.1%, respectively. The evaluation of the temperature profile inside the panel is essential to understand how heat is dissipated. The results show that the top surface (glass) is almost always colder than the back of the panel, despite being exposed to radiation. In addition, the upper surface dissipates more heat power than the lower one. Cooling systems, such as spray cooling, work better if they are installed on the back of the panel.

**Keywords:** thermal model; PV efficiency; heat dissipation; cloud cover; sky temperature



**Citation:** Nicoletti, F.; Cucumo, M.A.; Ferraro, V.; Kaliakatsos, D.; Gigliotti, A. A Thermal Model to Estimate PV Electrical Power and Temperature Profile along Panel Thickness. *Energies* **2022**, *15*, 7577. <https://doi.org/10.3390/en15207577>

Academic Editors: Abdul-Ghani Olabi, Michele Dassisti and Zhien Zhang

Received: 25 September 2022

Accepted: 11 October 2022

Published: 14 October 2022

**Publisher's Note:** MDPI stays neutral with regard to jurisdictional claims in published maps and institutional affiliations.



**Copyright:** © 2022 by the authors. Licensee MDPI, Basel, Switzerland. This article is an open access article distributed under the terms and conditions of the Creative Commons Attribution (CC BY) license (<https://creativecommons.org/licenses/by/4.0/>).

## 1. Introduction

Increasing the proportion of energy from renewable sources is a key element in reducing greenhouse gas emissions and keeping the average global temperature increase below 2 °C compared to pre-industrial levels. In fact, reducing the use of fossil fuels by replacing them with renewable resources contributes to the decarbonization of the energy system.

Energy communities are collective organizations that will help the transition to clean energy. They aim to use energy in the same place where it is produced, sharing it among several citizens and managing storage systems in a smart way. They make it possible to create energy-independent areas, with benefits for citizens and the health of the planet. In this context, photovoltaic (PV) fields play an important role. Predicting their electrical productivity is useful for managing their interconnection within a smart grid [1]. In order to optimize the operation of energy communities, it is very useful to be able to predict the energy demand of users, the electrical supplies of the generators and the charge levels of the electrical accumulators installed in the area [2–4]. Being able to simulate the thermal and electrical behavior of generation systems as a function of atmospheric conditions becomes important, especially if the primary source has variable availability, as in the case of solar source [5].

The estimation of producibility helps to understand whether the system solution is appropriate for the location or whether other types of installation are preferable [6], even to obtain only small advantages. Photovoltaic production can be increased in several ways, such as using panels that can rotate around an axis [7], using double-sided panels [8], or

through cooling methods [9]. Photovoltaic cells are the elements that convert solar radiation into electrical energy. The conversion efficiency is adversely affected by the temperature rise of the PV cells. This increase is associated with part of the absorbed solar radiation, which is converted into heat. The temperature reached by the cells is therefore an important factor to monitor. The need therefore arises to develop a mathematical model that is able to estimate the temperature field within a panel in a simple way.

Several authors proposed different methods for modelling PV modules as electrical circuits [10–15], many of them focusing on the PV cell model parameter estimation problem [11–15]. Saadaoui et al. [15] proposed a genetic algorithm to identify the parameters of photovoltaic panels. Abbassi et al. [16], used the Newton–Raphson method to determine the parameters of the PV panel. The model, then, was improved using a genetic algorithm. These studies aim to model the systems from an electrical point of view without assessing the thermal behavior of the panel.

The determination of the temperature of the photovoltaic cells is a different and very interesting problem, since the conversion efficiency of solar radiation into electrical energy depends on it. Sohani et al. [17] solved the thermal and electrical problem by focusing on the importance of the variation of thermophysical properties with temperature. They obtain interesting results, but the model is not quickly applicable as the temperatures are not known; therefore, a recursive method is required. Mavromatakis et al. [18] compared greatly simplified models that could be applied with a single equation. The results, however, have an excessive RMSE. They stated that a more complex method is needed to obtain more accurate results. Therefore, it can be useful to find the right compromise between implementation difficulty and accuracy.

Faiman D. [19] proposed a modified form of the Hottel–Whillier–Bliss equation, usually used for solar thermal collectors, in order to predict PV temperatures. Mattei M. et al. [20] proposed different simple models to estimate the PV temperature. The first uses the definition of NOCT and the others use the energy balance equation considering different correlations for the heat convective coefficient. They obtained a root-mean-square error (RMSE) of about 2.24 °C. Other simple methods to estimate the PV temperature were collected by Jakhrani et al. [21]. They observed that most models show quite distinct values when compared among each other. The best models are those based on the energy balance equations. However, all these methods have turned out to be simple and with low accuracy.

Ceylan et al. [22] used an artificial neural network to predict module temperature. Their experimental study concerned the training of ANN according to solar radiation and air temperature detected in Turkey. For this investigation, ambient temperature was kept constant at values of 10, 20, 30 and 40 °C and the network cannot provide accurate results under conditions other than those used for training, including panel inclination and wind speed. Aly et al. [23] and Bevilacqua et al. [24] proposed a finite difference method to estimate the temperature profile. They managed to obtain very accurate results, but the method used is complex to implement because it divides the panel into numerous nodes. In the present study, a simpler finite difference approach will be used, using only the strictly necessary nodes, one for each layer. In this way, the model will be easily replicable, while maintaining good accuracy in the results.

Moreover, none of the previous studies considered the cloudiness of the sky to estimate the equivalent temperature of the celestial vault. This is an important parameter influencing radiative heat exchange that is often not measured and therefore cannot be used as input. The present work provides a method for estimating cloud cover using solar irradiance already considered as input.

The aim of this study is to develop a simple calculation method to determine the temperature profile inside the PV panel and to provide information on heat dissipation. The code will be experimentally validated with data acquired at the laboratory of the University of Calabria. The model implements the energy balance equations of the layers also considering the capacitive terms. Developing a non-stationary model allows good results to be obtained even when atmospheric conditions change suddenly, for example,

when a cloud passes. Furthermore, it allows the energy balance equations to be solved in a non-recursive manner, evaluating temperatures at the next moment. The model will later be used to derive information about the role played by each layer in heat dispersion. This aspect is important because it helps to choose the best strategy in case a cooling system is to be implemented.

The rest of the paper proceeds as follows; in Section 2, the methodology to estimate the temperature profile is shown and the method to estimate the cloud cover is proposed. After providing information on the experimental setup, the model is validated in Section 3. Useful results for understanding the heat loss in the panel will then be shown. Finally, in Section 4, the results obtained are discussed.

## 2. Materials and Methods

### 2.1. Thermal Model

The typical structure of a photovoltaic panel consists of five layers: glass, EVA, PV cell, EVA and insulation. Each of them behaves differently with respect to heat transfer. To simulate their behaviour when exposed to solar radiation, each layer is thermally modelled using energy balance equations. Spatial discretization is performed by dividing the panel into five nodes which are representative of the single layers.

Figure 1 shows the stratigraphy of the panel and its division into nodes. The first point of the spatial discretization is fixed on the top surface of the glass layer. The temperature of this point is called  $T_{fg}$ . The next point is fixed in the center of the EVA (Ethylene Vinyl Acetate) layer and its temperature is  $T_{ev,sup}$ . The photovoltaic layer is modelled through a central node and the associated temperature is  $T_{pv}$ . The next point is in the center of the EVA layer that divides it from the thermal insulation and its temperature is called  $T_{ev,inf}$ . Finally, the last one representing the thermal insulating tedlar (polyvinyl fluoride) layer is placed on the lower surface and its temperature is called  $T_{ted}$ . The top and bottom nodes are placed on the edges of the layers and not in the middle to facilitate data processing. These collocations, in fact, allow the temperatures at the extremities to be directly evaluated directly by solving the balance equations. These nodes are, however, still representative of the entire layer on which they are placed, both with reference to the calculation of thermal capacitances and conductive resistances. Figure 1 also shows names assigned to the thicknesses of the layers.

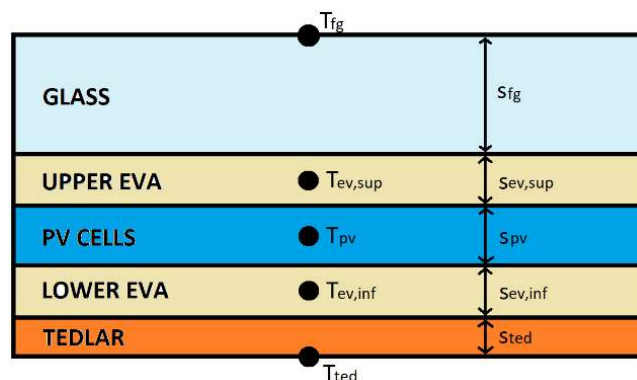


Figure 1. Stratigraphy of the PV panel and nodes.

The nodes inside the panel exchange heat only by conduction with adjacent nodes. The nodes at the ends, on the other hand, also exchange heat by convection with the outside air and by radiation with the sky and ground. Incident global irradiance  $G$  is absorbed by the front glass and PV cells, in proportion to their absorption coefficient. Accumulated power also appears in the equations because the problem is time-variant. The problem is solved using the finite difference (FD) discretization technique. The derivative terms are

therefore discretized in a finite time interval,  $\Delta t$ . The equations, written for the defined nodes, are:

$$h_c(T_a - T_{fg}) + h_{r,fg \rightarrow sky}(T_{sky} - T_{fg}) + \frac{T_{ev,sup} - T_{fg}}{R_{fg} + \frac{1}{2}R_{ev}} + h_{r,fg \rightarrow gr}(T_{gr} - T_{fg}) + \alpha_{fg}G = C_{fg} \frac{T_{fg} - {}^p T_{fg}}{\Delta t} \quad (1)$$

$$\frac{T_{fg} - T_{ev,sup}}{R_{fg} + \frac{1}{2}R_{ev}} + \frac{T_{pv} - T_{ev,sup}}{\frac{1}{2}R_{ev} + \frac{1}{2}R_{pv}} = C_{ev} \frac{T_{ev,sup} - {}^p T_{ev,sup}}{\Delta t} \quad (2)$$

$$\frac{T_{ev,sup} - T_{pv}}{\frac{1}{2}R_{ev} + \frac{1}{2}R_{pv}} + \frac{T_{ev,inf} - T_{pv}}{\frac{1}{2}R_{pv} + \frac{1}{2}R_{ev}} + \alpha_{PV} \cdot \tau_{fg} \cdot G \cdot (1 - \eta_{PV}) = C_{pv} \frac{T_{pv} - {}^p T_{pv}}{\Delta t} \quad (3)$$

$$\frac{T_{pv} - T_{ev,inf}}{\frac{1}{2}R_{pv} + \frac{1}{2}R_{ev}} + \frac{T_{ted} - T_{ev,inf}}{\frac{1}{2}R_{ev} + R_{ted}} = C_{ev} \frac{T_{ev,inf} - {}^p T_{ev,inf}}{\Delta t} \quad (4)$$

$$h_c(T_a - T_{ted}) + h_{r,ted \rightarrow sky}(T_{sky} - T_{ted}) + \frac{T_{ev,inf} - T_{ted}}{\frac{1}{2}R_{ev} + R_{ted}} + h_{r,ted \rightarrow gr}(T_{gr} - T_{ted}) = C_{ted} \frac{T_{ted} - {}^p T_{ted}}{\Delta t} \quad (5)$$

where  $R_i$  is the thermal resistance of the  $i$ -th layer, defined by the ratio of the thickness  $s_i$  to the thermal conductivity  $k_i$ ;  $C_i$  is the heat capacity per unit area of the  $i$ -th layer, defined by the product of specific heat  $c_i$  density  $\rho_i$  and thickness  $s_i$ . The optical properties appearing in the equations are  $\alpha$  and  $\tau$ , which represent the absorption and transmission coefficients, respectively. EVA layers are considered to be perfectly transparent to solar radiation. Moreover, solar radiation absorbed by the tedlar is considered negligible. The electrical efficiency  $\eta_{PV}$  depends on the incident irradiance and on the cell temperature  $T_{pv}$ . It is obtained with the Evans equation [25]:

$$\eta_{PV} = \eta_{PV,R} \cdot \left[ 1 - \beta_R(T_{pv} - T_R) + \gamma \log_{10} \frac{G}{1000} \right] \quad (6)$$

where  $\beta_R$  is  $0.006 \text{ } ^\circ\text{C}^{-1}$  and  $\gamma$  is 0.085 for monocrystalline silicon panels. The temperature of standard reference conditions  $T_R$  for performance classification is  $25 \text{ } ^\circ\text{C}$ . The subscript  $R$  refers to quantities acquired under standard test conditions.

The unknowns are the temperatures at the current instant. Temperatures with apex  $p$  are already known as they are calculated at the previous time instant. The input data required to apply the model are the ambient temperature, wind speed and global irradiance incident on the tilted plane. Convective and radiative heat transfer coefficients are determined using the following procedure.

## 2.2. Heat Transfer Coefficients

Convective heat transfer coefficients are determined by considering both natural and forced contributions. The correlation used to combine the two effects is provided by Churchill [26]:

$$h_c = \sqrt[3]{h_{c,n}^3 + h_{c,f}^3} \quad (7)$$

With reference to natural convection, the convective coefficient is determined using the correspondent formulations of the Nusselt number [27]. The equation for the upper surface is:

$$Nu_n = 0.13 \cdot Ra^{\frac{1}{3}} \quad (8)$$

while for the lower surface, it is:

$$Nu_f = 0.27 \cdot Ra^{\frac{1}{4}} \quad (9)$$

The length used for the calculation of the Rayleigh number  $Ra$  is the average length of the two main dimensions of the panel: length  $L_1$  and width  $L_2$ . The convective heat transfer coefficient is therefore deduced from the definition of the Nusselt number.

$$h_{c,n} = \frac{k_{air} Nu_n}{\frac{L_1+L_2}{2}} \quad (10)$$

With reference to forced convection, the equations for determining the Nusselt number depend on the type of flow and are considered equal for the upper and lower surface. In the case of turbulent flow, the Nusselt number is a function of Reynolds  $Re$  and Prandtl  $Pr$  numbers [28]:

$$Nu_f = 0.86 \cdot Re_{L_c}^{\frac{1}{2}} \cdot Pr^{\frac{1}{3}} \quad (11)$$

where the characteristic length  $L_c$ , used to calculate the  $Nu$  and  $Re$  number, is:

$$L_c = \frac{4 L_1 L_2}{2 (L_1 + L_2)} \quad (12)$$

In conditions of forced convection with laminar outflow, the classical expression is used [29]:

$$Nu_f = 0.664 \cdot Re_{L_c}^{\frac{1}{2}} \cdot Pr^{\frac{1}{3}} \quad (13)$$

Finally, the convective coefficient can be determined.

$$h_{c,f} = \frac{k_{air} Nu_f}{L_c} \quad (14)$$

In order to determine the heat transfer coefficients for radiation, the non-linearized analytical formulas are used for both the lower and upper surfaces:

$$h_{r,i \rightarrow j} = \frac{\sigma \cdot (T_i^2 + T_j^2) (T_i + T_j)}{\frac{1-\varepsilon_i}{\varepsilon_i} + \frac{1}{F_{i \rightarrow j}}} \quad (15)$$

where the subscript  $i$  can represent the upper surface or the lower surface and the subscript  $j$  can represent the sky or the ground. The view factors are:

$$F_{fg \rightarrow sky} = F_{ted \rightarrow gr} = \frac{1 + \cos\beta}{2} \quad (16)$$

$$F_{fg \rightarrow gr} = F_{ted \rightarrow sky} = \frac{1 - \cos\beta}{2} \quad (17)$$

The ground temperature is set equal to the ambient temperature:

$$T_{gr} = T_a \quad (18)$$

Sky temperature is an important quantity to set as it influences heat exchange by radiation. Results obtained with different sky temperature models will be compared. The first method was proposed by Grag [30]. The temperature of the sky is obtained by reducing the ambient air temperature by 20 degrees.

$$T_{sky} = T_a - 20 \quad (19)$$

The second method considered is provided by Swinbank [31]:

$$T_{sky} = 0.0552 \cdot T_a^{1.5} \quad (20)$$

where the temperatures are expressed in Kelvin. The last method is an integration of the previous one [32]. The sky temperature is a function of the air temperature  $T_a$  and cloud cover  $N$  expressed in octaves of the sky covered by clouds:

$$T_{sky} = 0.0552 \cdot T_a^{1.5} + 2.625 \cdot N \quad (21)$$

### 2.3. Proposed Model for Estimating Sky Cloudiness

To apply Equation (21), it is necessary to estimate the cloudiness of the sky. Sky conditions are defined by how many eighths are covered by clouds. It is difficult, with the help of low-cost sensors, to be able to determine the cloudiness of the sky, yet it has a significant influence on the radiative heat exchange. Therefore, a method is proposed to estimate the cloud cover. It consists of making a comparison with the irradiance of clear sky conditions estimated by the ASHRAE model [33]. The theoretical global irradiance  $G_t$  for a clear day is:

$$I_{bn} = C_1 e^{-C_2 / \sin \theta_s} \quad (22)$$

$$I_{do} = C_3 I_{bn} \quad (23)$$

$$G_t = I_{bn} \cos i + I_{do} F_{fg \rightarrow sky} + (I_{bn} \sin \theta_s + I_{do}) \rho_{gr} F_{fg \rightarrow gr} \quad (24)$$

in which  $C_1$ ,  $C_2$  and  $C_3$  are tabulated values based on the period of the year [33],  $\rho_{gr}$  is the albedo taken equal to 0.2,  $\theta_s$  is the solar altitude,  $I_{bn}$  is the direct normal irradiance,  $I_{do}$  is the diffuse irradiance on the horizontal plane,  $i$  is the incidence angle. The method for estimating cloud cover consists in comparing the real measured irradiation  $G$  with the theoretical one for clear day  $G_t$ . The proposed formulation is the following, where the numerical values are obtained during the validation phase:

$$N = \begin{cases} 0 & \text{if } G/G_t > 0.6 \\ 8(1 - G/G_t) & \text{if } 0.1 < G/G_t < 0.6 \\ 8 & \text{if } G/G_t < 0.1 \end{cases} \quad (25)$$

To avoid slight transient phenomena, the cloud cover is then adjusted by making time averages over one-hour timesteps. The advantage of this model is that it allows the sky cloudiness to be estimated with reference only to the portion of the sky seen by the panel based on its inclination. The cloudiness of the portion of the sky not seen by the panel, whose cloudiness has no influence on radiative exchange, is therefore not considered.

### 2.4. Experimental Setup

The data used to validate the theoretical model were taken at the Solar Energy Laboratory of DIMEG at the University of Calabria (latitude 39.37 °N, longitude 16.23 °E). The photovoltaic panel is Schüco MPE 245 PG 60 FA. The size of the panel is 1663 × 998 mm and its inclination is 30° towards the South (Figure 2). The nominal power of the panel is 245 W and the reference yield declared by the manufacturer  $\eta_{PV,R}$ , evaluated under standard conditions, is 14.5%. The NOCT is 43 °C. The thermophysical characteristics of the panel layers are listed in Table 1 [30].

The temperature is measured by means of Pt 100 1/3 sensors with an error of 0.1 °C positioned on the back of the panels. The solar irradiance is measured directly on the inclined plane by means of a SMP3 Kipp&Zonen pyranometer with a non-linearity of 0.5% and uncertainty of 2%. The wind speed is measured with uncertainty of 2.5%. The experimental data used were acquired in January 2016 and July 2016 with a timestep of 1 min. The absorption coefficients of glass  $\alpha_{fg}$  and photovoltaic cells  $\alpha_{PV}$  are 0.05 and 0.93 respectively; the glass transmission coefficient  $\tau_{fg}$  is 0.9; the emissivity values of glass  $\varepsilon_{fg}$  and tedlar  $\varepsilon_{ted}$  are both 0.85.



**Figure 2.** Experimental set-up at DIMEG—Unical.

**Table 1.** Thermophysical characteristics of the layers.

	Thickness (mm)	Thermal Conductivity (W/mK)	Density (kg/m <sup>3</sup> )	Specific Heat (J/kgK)
Glass	3.2	1.8	3000	500
Upper EVA	0.2	0.35	960	2090
PV cells	0.3	148	2330	677
Lower EVA	0.2	0.35	960	2090
Tedlar	0.1	0.2	1200	1250

### 2.5. Performance Metrics

The parameters that will be used to validate the model are: the Pearson correlation coefficient  $r_{xy}$ , the mean bias error (MBE), the root-mean-square error (RMSE), the normalized root-mean-square error (NRMSE), and the Nush–Sutcliffe Efficiency (NSE). These indices will be calculated on minute-by-minute data and are defined by the following equations, where  $x$  and  $y$  are the calculated and experimental quantities respectively.

$$r_{xy} = \frac{\sum(x_i - x_{ave}) \cdot (y_i - y_{ave})}{\sqrt{\sum(x_i - x_{ave})^2} \cdot \sqrt{\sum(y_i - y_{ave})^2}} \quad (26)$$

$$MBE = \frac{\sum(x_i - y_i)}{N} \quad (27)$$

$$RMSE = \sqrt{\frac{\sum(x_i - y_i)^2}{N}} \quad (28)$$

$$NRMSE = \frac{1}{y_{max} - y_{min}} \sqrt{\frac{\sum(x_i - y_i)^2}{N}} \quad (29)$$

$$NSE = 1 - \frac{\sum(x_i - y_i)^2}{\sum(y_i - y_{ave})^2} \quad (30)$$

where  $x_{ave}$  is the average of  $x$ ,  $y_{ave}$  is the average of  $y$ ,  $y_{max}$  and  $y_{min}$  are the maximum and minimum values recorded.

## 3. Results

### 3.1. Validation of Sky Temperature Model

The equations are solved by determining the temperatures progressively at the next instant of time. The time interval considered for time discretization is 1 min in analogy with the acquisition of experimental data. The equations are structured in such a way that the system is solved in the “implicit mode” and the time interval does not generate

problems of instability of the solution. The model used to determine the sky temperature has a considerable influence on the results. In order to determine the best model for estimating the sky temperature, the formulations usually used in the literature and the one proposed by this study were considered. Figure 3 shows, as an example for 26 July, the comparison between the temperature values obtained for tedlar and the experimental values measured. The first model is based only on a reduction of 20 °C in the ambient temperature and approximates the results worse than the others. The day in question was cloudy at certain times in the afternoon. The Swinbank model and the proposed model show identical solutions in the morning hours, i.e., with clear skies. In the afternoon, due to the cloudiness of the sky, the panel temperature decreases. The proposed model, under these circumstances, provides a more accurate solution than the simplified model. It is able to recognize the cloudiness and a higher temperature is assigned to the sky, which reduces the radiative heat exchange with the PV panel. Figure 4 shows the root-mean-square error on the temperature obtained with reference to the measurements for the entire months of January and July. The proposed model allows the error to be reduced compared to the other methods usually used in the literature, obtaining an RMSE of 1.84 °C.

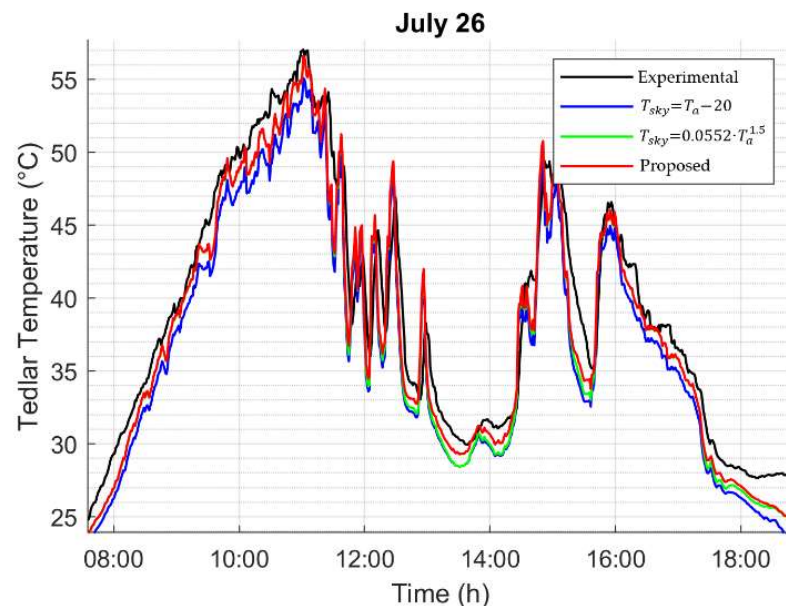


Figure 3. Temperature of tedlar for different sky temperature models.

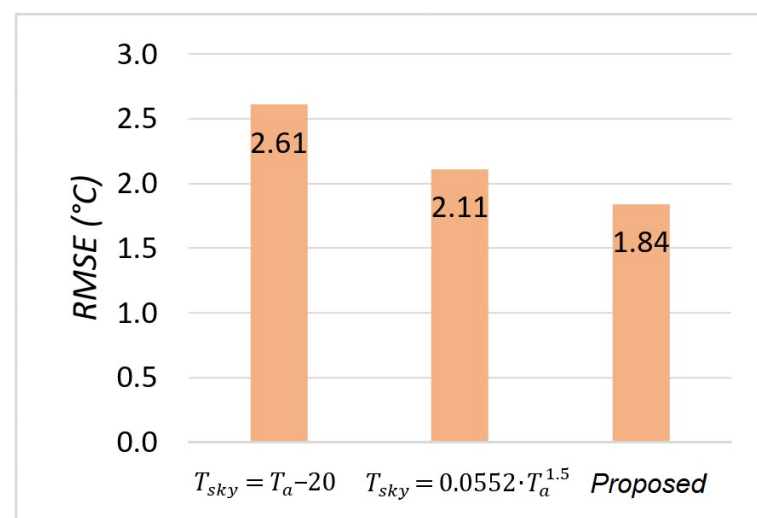
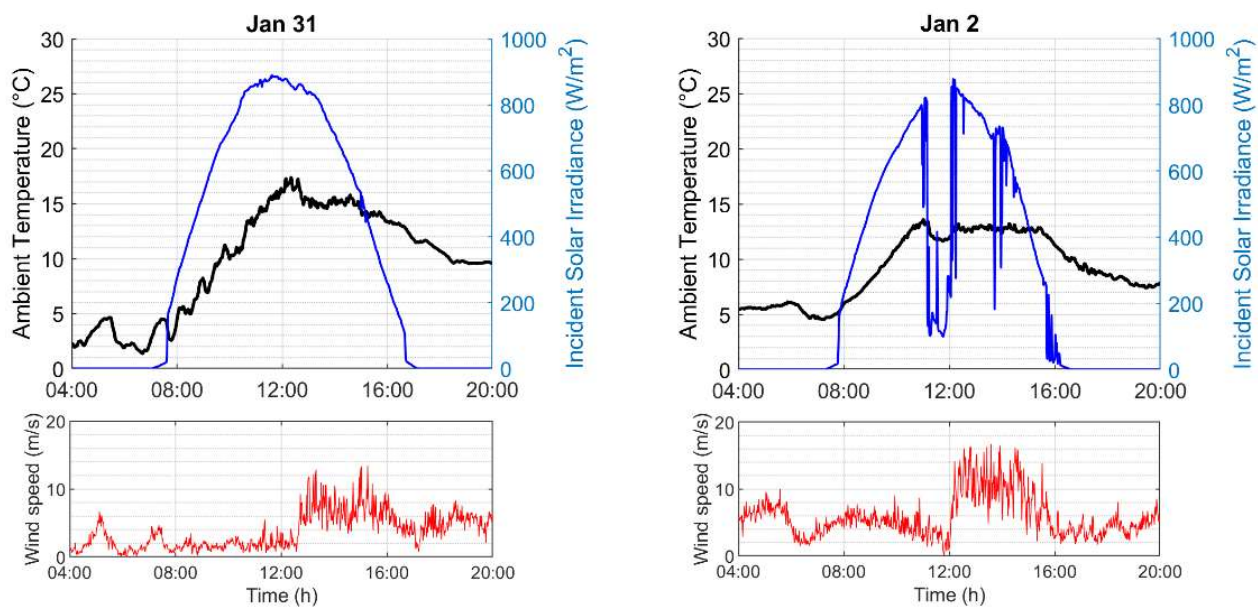


Figure 4. Temperature RMSE for different sky temperature models.

The model that will now be used to estimate the sky temperature will be the one proposed. Validation of the model will be conducted via winter and summer operation, with reference to both clear and cloudy days, with weak and strong winds.

### 3.2. Validation in Winter Conditions

The results obtained for a clear winter day (31 January) and an overcast winter day (2 January) are analyzed to validate the model. The climatic conditions are shown in Figure 5. The figure shows, on the left, the data for 31 January, which was a clear day, as can be seen from the solar radiation curve. On the right, the figure shows the climate data for 2 January, which was cloudy in the middle of the day and at certain times in the afternoon. During 31 January, the thermal variation was greatest; on 2 January the air temperature fluctuated between 5 and 14 °C and there was a reduction between 11:00 and 12:00, when the sky was cloudy. At the bottom, the figure shows the trends of wind speed, which was low in the morning for both days and then rose in the afternoon. These two days have been chosen because the wind was very variable and, therefore, it is possible to monitor the results with reference to flow conditions that can be laminar or turbulent.



**Figure 5.** Ambient temperature, solar irradiance, and wind speed on 31 January and 2 January.

Therefore, the sky was cloudy between 11:00 and 12:00 on 2 January. We do not know if a small cloud covered only the solar disk or if the whole sky was cloudy. To avoid minor transient phenomena, the cloud cover is estimated by averaging it over one hour. Figure 6 shows the percentage of cloud cover estimated with the proposed model. It can be noted that high cloud cover is observed in the central hours of the day, while at 14:00, the percentage of cloud cover is shown to be very low. In fact, the sky was probably not half-covered as it would appear from the reduction in solar irradiance, but a passing cloud may have covered only the solar disk. Thanks to the temporal averages, the cloud cover is about 85% in this first case, and it is less than 5% at 14:00. Before sunrise and after sunset, when the sun is not in the sky, the values are not of interest to us. However, in these cases, cloud cover is less accurately estimated based on the relative humidity value.

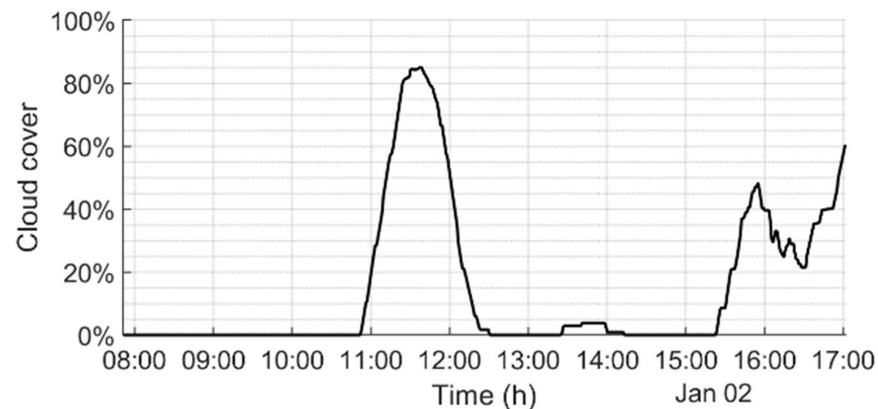


**Figure 6.** Cloud cover percentage on 2 January.

The values of tedlar temperature, electrical power, and electrical efficiency are shown in Figure 7. The latter is calculated using Equation (6). The electrical power is obtained with the following equation:

$$P_{el} = \eta_{PV} \cdot G \quad (31)$$

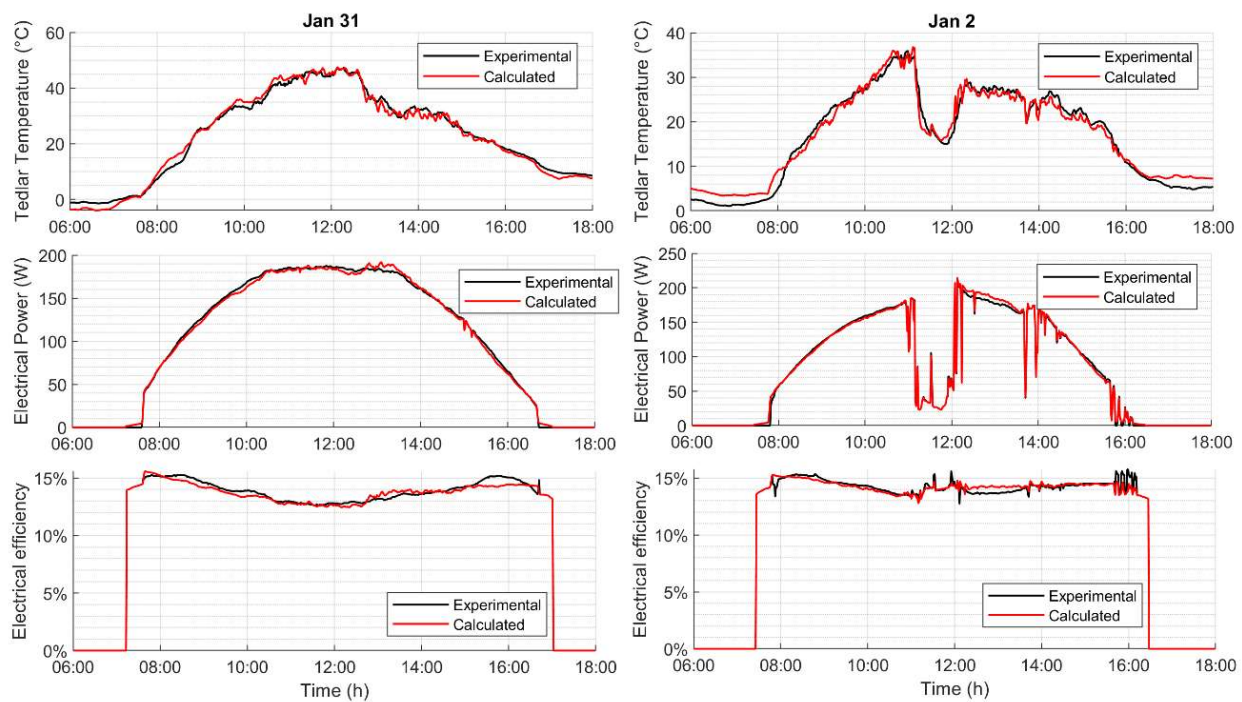


**Figure 7.** Tedlar Temperature, Electrical Power and Efficiency for a clear day and overcast day.

The highest temperature value was reached on the clear day around noon and was 47.4 °C. From 12:30 onwards, there was a drastic drop in temperature, presumably due to the increase in the wind speed. In the early afternoon it was constant and around 30 °C. On the overcast day, on the other hand, the temperature started to decrease from 11:00 onwards as the radiation decreased. The values obtained from the mathematical model are very similar to those measured. The statistical parameters also confirm this qualitative consideration (Table 2). In particular, the correlation coefficient CC is very high in both cases: over 0.99. The Nash–Sutcliffe efficiency (NSE) for the clear day is 0.989, which means that the accuracy of the model is excellent. It is slightly worse on the overcast day (0.964). The Mean Bias Error (MBE) is slightly negative, and this denotes a slight underestimation of the simulated data compared to the real ones. The root-mean-square error (RSME) is approximately 1.7 °C for the clear day and 1.8 °C for the overcast day.

**Table 2.** Experimental validation indices for winter conditions.

		$r_{xy}$	MBE (°C)	RMSE (°C)	NRMSE	NSE
Tedlar Temperature	Clear day	0.996	−0.602	1.694	3.5%	0.989
	Overcast day	0.992	−0.725	1.807	4.9%	0.964
		$r_{xy}$	MBE (W)	RMSE (W)	NRMSE	NSE
Electrical Power	Clear day	0.9995	−0.512	2.476	1.2%	0.999
	Overcast day	0.9992	0.406	2.876	1.4%	0.998
		$r_{xy}$	MBE (%)	RMSE (%)	NRMSE	NSE
Electrical Efficiency	Clear day	0.9994	−0.081	0.268	1.7%	0.998
	Overcast day	0.9985	−0.023	0.387	2.5%	0.997

With reference to the electrical power, the experimental values are well matched. It is only in the early afternoon that the estimated electrical power was slightly higher than the actual power for both days considered. This is due to the slight underestimation of the temperature in the same time slot. The statistical parameters confirm the good approximation of the model. The correlation index and the NSE are very high. The MBE is about half a Watt, and it is negative for the clear day and positive for the overcast day. The root-mean-square error is less than 3 W.

The electrical efficiency varies between 12 and 15% and this is confirmed by the experimental data. The statistical indices show, again, that the model adequately approximates the actual data. At 16:00 on 2 January, the model shows a fluctuation in electrical efficiency. The experimental data do not agree with the prediction, as the actual oscillation is greater. These errors are usually present at dawn and dusk, when, in any case, electricity production is low.

### 3.3. Validation in Summer Conditions

The summer validation is referred to 11 July and 23 July. Again, these represent a clear day and an overcast day. The global irradiance, ambient temperature and wind speed are shown in Figure 8. During the clear day, the temperature varied between 20 and 35 °C, and decreased in the afternoon due to high wind speeds. On 23 July it reached a maximum of about 32.5 °C around 10:00 and decreased first due to high wind speeds and, in the afternoon, due to the absence of solar radiation. The days, again, were chosen with varying wind speeds throughout the day.

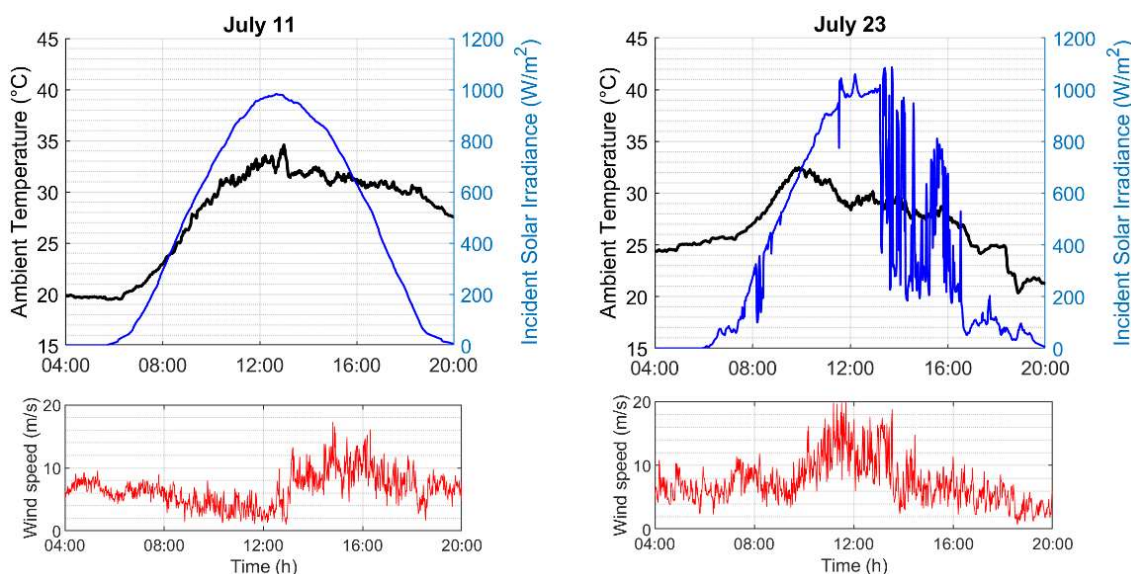


**Figure 8.** Ambient temperature, solar irradiance, and wind speed on 11 July and 23 July.

The percentage cloud cover estimated for 23 July is shown in Figure 9. The sky is estimated to have been slightly overcast in the early morning hours (07:00–09:00), and two peaks of cloudiness are identified in the afternoon equal to 49 and 77%.

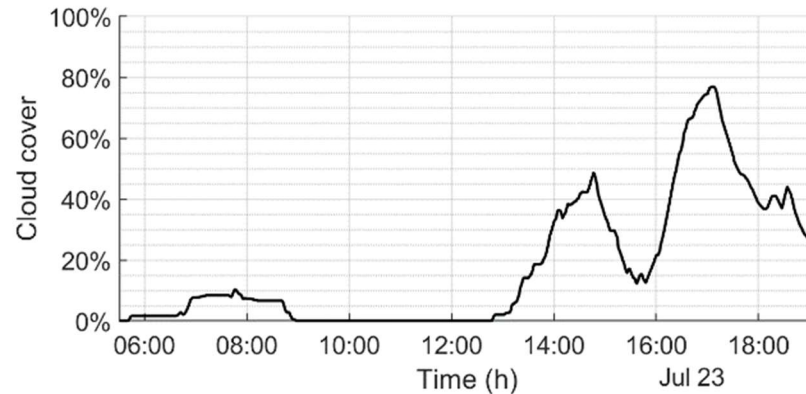


Figure 9. Cloud cover percentage on 23 July.

The tedlar temperatures are shown in Figure 10. On 11 July, the maximum value reached was about 65 °C, well identified by the model. After 13:00, the temperature suddenly dropped to around 50 °C due to the turbulent flow generated by the high-velocity air. On 23 July, the panel cooled down slightly in the afternoon due to the reduction in solar irradiation. The model behaves adequately but, in this case, is less accurate than on the clear day. The correlation indexes are 0.996 for clear day and 0.983 for overcast day (Table 3). The NSE also decreases in the case of overcast day, passing from 0.99 to 0.957. The MBE indicates that, in both cases, the data are slightly underestimated. The root-mean-square error is 1.4 °C for the clear day and 2.25 °C for the overcast day.

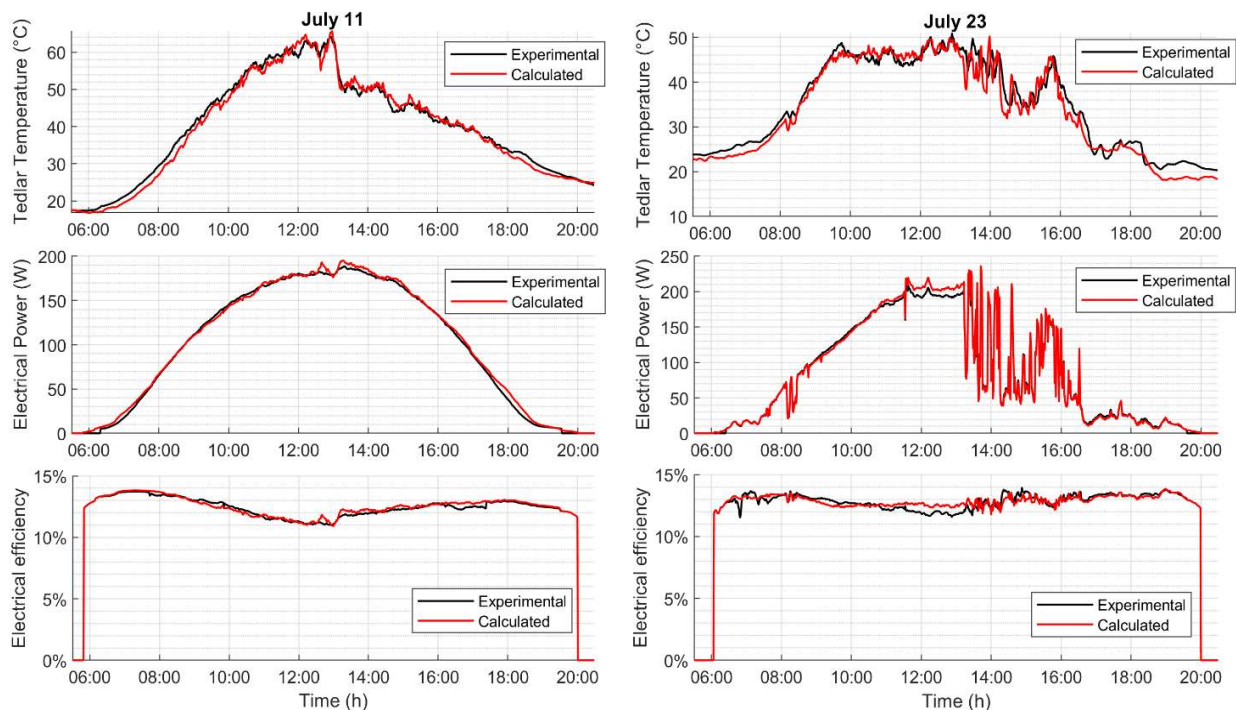


Figure 10. Tedlar Temperature, Electrical Power and Efficiency for a clear day and overcast day.

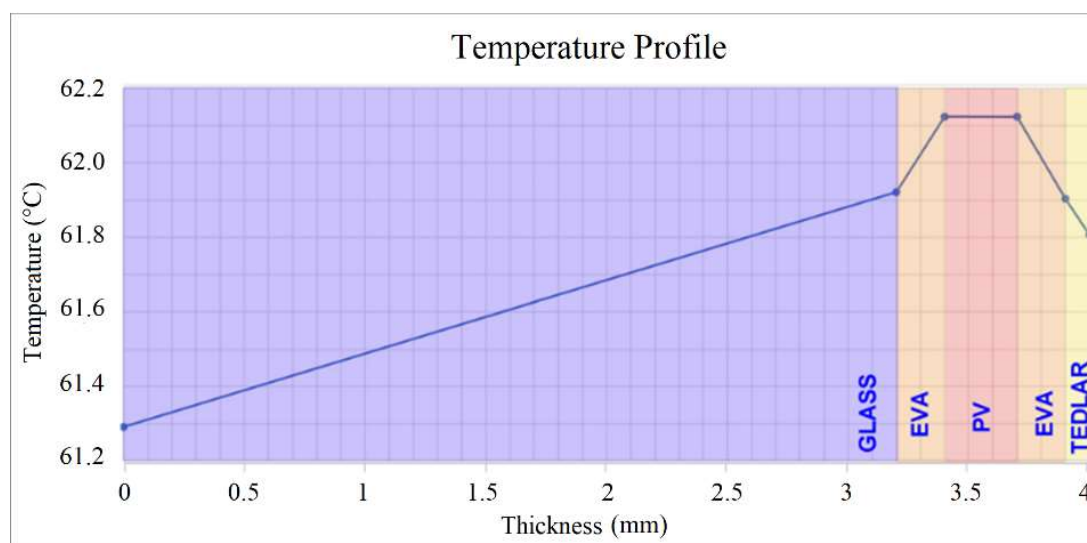
**Table 3.** Experimental validation indices for summer conditions.

		$r_{xy}$	MBE (°C)	RMSE (°C)	NRMSE	NSE
Tedlar Temperature	Clear day	0.996	−0.513	1.442	3.3%	0.990
	Overcast day	0.983	−1.036	2.248	7.1%	0.957
Electrical Power		$r_{xy}$	MBE (W)	RMSE (W)	NRMSE	NSE
	Clear day	0.9992	1.713	3.391	1.8%	0.998
Overcast day	0.9990	1.642	4.264	2.1%	0.997	
Electrical Efficiency		$r_{xy}$	MBE (%)	RMSE (%)	NRMSE	NSE
	Clear day	0.994	0.077	0.239	1.7%	0.987
Overcast day	0.988	−0.147	0.757	5.3%	0.974	

The model predicts electrical output quite well, especially when irradiance is highly variable. For the clear day, the MBE is +1.7 W and RMSE is 3.4 W. CC and NSE are, instead, excellent. The model slightly overestimates electricity production at noon. With reference to the electrical efficiency, the NSE is about 0.98. For the overcast day, on the other hand, the MBE is about the same as in the previous case, but with a higher RMSE. Again, there is an overestimation at midday, although the temperature is well identified at this time.

### 3.4. Temperature Profile along Panel and Influence on Heat Dispersion

Figure 11 shows the temperature profile within the entire panel assessed by the model at 12:00 on 11 July. The outside air temperature is 34.6 °C, the global irradiance measured on the panel plane is 978 W/m<sup>2</sup> and the wind speed is 7.1 m/s.

**Figure 11.** Temperature of the panel at noon of 11 July.

Thanks to the model, it is possible to calculate the temperatures of the nodes for which the balance equations were written. It is possible, moreover, to identify the temperatures at the layer interfaces using a simple electrical analogy. Figure 11 shows that temperature is almost uniform within the panel, oscillating between 61.3 and 62.1 °C. The hottest component is the PV layer, while the coldest one is the outer surface of the glass, despite being directly exposed to sunlight. The temperatures on the two sides of the panel are different. It may seem anomalous that the temperature in the tedlar surface is higher than that in the glass surface. Tedlar, in fact, is a thermal insulator and it was expected that the temperature of its outer face could be close to the temperature of the air (or at least lower than the temperature of the face of the glass, which is also directly exposed to the sun's rays).

The graphs in Figure 12 correlate the temperature difference between the PV layer and both the surfaces of the front glass and tedlar with the irradiation values. The figure shows that the internal temperature gradients are linearly proportional to the irradiance  $G$

incident on the panel. The evidence found on 11 July at noon (tedlar temperature higher than glass temperature) is confirmed under all operating conditions.

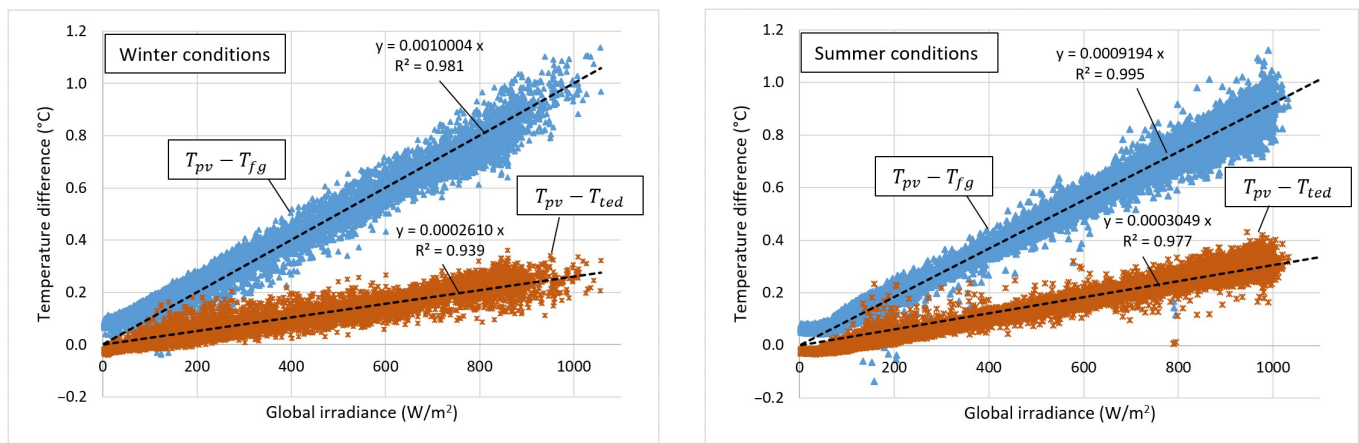


**Figure 12.** Temperature difference between PV layer and front glass/tedlar surfaces. Winter and summer conditions.

In fact, blue dots in the figure are almost always placed higher than the orange dots. Only for a few points, in low irradiation conditions, is there an overlap between the two areas. In these few cases it may result in the temperature of the glass being higher than the temperature of the tedlar.

The figure distinguishes between winter and summer conditions. With reference to winter conditions, the temperature difference  $T_{pv} - T_{fg}$  is linearly linked with global irradiance by means of the correlation  $y = 0.0010004 \cdot x$ , with  $R^2 = 0.981$ . The temperature difference, instead, between the PV layer and the tedlar surface is linked with global irradiance by means of the equation  $y = 0.0002610 \cdot x$ , with  $R^2 = 0.939$ . On average, therefore, the temperature deviation with tedlar is four times lower than with the front glass surface. In summer operating conditions, the graph is similar to the previous one and the linear proportionality with the global irradiance is confirmed. The interpolating equations change slightly. With reference to the temperature difference between the PV layer and the front glass, the equation is  $y = 0.0009194 \cdot x$ , with  $R^2 = 0.995$ ; the temperature difference with the tedlar, on the other hand, has a correlation of  $y = 0.0003049 \cdot x$ , with  $R^2 = 0.977$ . The equations are quite similar between the winter and summer case, but in the latter case it turns out that the temperature difference with the tedlar is about three times smaller than the temperature difference with the front glass.

The glass surface is therefore cooler than the back of the panel. However, this does not mean that it dissipates less heat by convection and radiation. On the contrary, the graphs in Figure 13 show that it is the cooler of the two surfaces (the front glass) and dissipates the most heat, under all conditions. The figure shows the trends of  $\dot{Q}_{fg}$  and  $\dot{Q}_{ted}$  indicating the thermal power lost to the outside by convection and radiation from the front glass and tedlar, respectively. The negative values of  $\dot{Q}_{ted}$ , recorded in the morning and evening, represent the moments when the air temperature was higher than the surface; here, the back of the panel is heated by the air, by radiation, and by the environment. Heat loss is greatly influenced by wind speed. In fact, the fluctuating trends are caused by the varying wind intensity.  $\dot{Q}_{fg}$  is always higher than  $\dot{Q}_{ted}$  by about 50–100 W/m<sup>2</sup>. In the summer period, the behavior is similar; however, the differences between the two curves are slightly smaller.

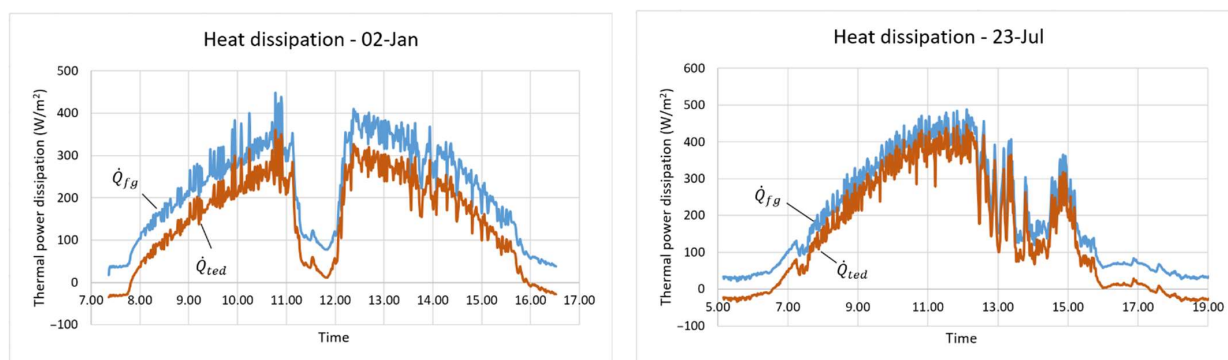


**Figure 13.** Temperature difference between PV cells and front glass/teflar surfaces. Winter and summer conditions.

#### 4. Discussion

The model allows temperature results to be estimated with simple methodology and good accuracy. The overall RMSE obtained for temperature is  $1.84\text{ }^{\circ}\text{C}$ . This result is lower than that of other works in the literature, such as Mavromatakis et al. [19] ( $\sim 2.1\text{--}2.2\text{ }^{\circ}\text{C}$ ) and Mattei et al. [21] ( $2.24\text{ }^{\circ}\text{C}$ ). The error is greater when compared to more complex methods. For example, Bevilacqua et al. [30] and Aly et al. [23] obtained an RMSE of  $1.37\text{ }^{\circ}\text{C}$  and between  $0.94$  and  $1.35\text{ }^{\circ}\text{C}$  respectively by using numerous nodes to discretize the PV panel. The methodology presented in this paper for estimating cloud cover has given very good results. It is based on the comparison between the measured irradiance and the theoretical irradiance under clear sky conditions. It has made it possible to reduce the RMSE temperature from  $2.11$  to  $1.84\text{ }^{\circ}\text{C}$ .

The study provided a simple method for estimating the performance of a PV panel. In addition, the proposed new sky temperature relationship can be used for research purposes in the photovoltaic and other fields.

The temperature profile shows that the highest temperature is reached by the PV cell. However, the temperature remains quite homogeneous within the entire panel: the maximum gradient is about  $1\text{ }^{\circ}\text{C}$ . This characteristic allows an easier thermal dispersion of the absorbed heat. The temperature of the glass is cooler than the temperature of the back of the panel. In addition, the upper surface dissipates more heat power than the lower surface. The study, therefore, suggests that any cooling system should be applied on the back side to increase heat exchange.

#### 5. Conclusions

The paper presented a simple one-dimensional transient model for estimating the temperature profile in a PV panel and the electrical power generated. The results were experimentally validated using a PV panel and the appropriate sensors placed on the 45/C building of the DIMEG at University of Calabria. The validation was carried out under both clear and overcast conditions, for both winter and summer days. In order to simulate overcast days, a methodology is proposed and validated for recognizing cloud cover. This information is necessary as it has a significant influence on the radiative heat exchange.

The model is able to predict the temperature of the back of the panel with an RMSE of about  $1.5\text{--}2.0^{\circ}$ . The RMSE on the estimation of the delivered electrical power is  $2.5\text{--}4.3\text{ W}$ . The RMSE on the electrical conversion efficiency is  $0.25\text{--}0.75\%$ . In both summer and winter periods, the MBE on the temperature estimation is negative, with values ranging between  $-1.0\text{ }^{\circ}\text{C}$  and  $-0.5\text{ }^{\circ}\text{C}$ . This means that the model returns slightly lower values than the real ones. The limitation of the present study is that the problem is considered one-dimensional. The temperature obtained is assumed homogeneous for the faces. This methodology does not allow for the evaluation of edge effects and does not consider the nonuniformity of the photovoltaic layer. However, the errors are acceptable because they are often lower than errors obtained through other scientific studies using more complex models.

The study found that the back of the panel reaches high temperatures and dissipates less thermal power than the front face. Facilitating cooling of the back face could be a useful solution to keep cell temperatures lower and improve panel efficiency. For this role, an effective solution is spray cooling, which involves spraying water mist droplets on the surface and waiting for them to evaporate by absorbing the latent heat of evaporation. The study shows that this solution should be adopted on the back face instead of the front face, and a study of its effectiveness represents a possible future development for this work.

**Author Contributions:** Conceptualization, F.N. and A.G.; methodology, F.N. and A.G.; software, A.G.; validation, F.N. and A.G.; formal analysis, F.N., D.K., V.F.; investigation, M.A.C., A.G. and D.K.; resources, F.N. and V.F.; data curation, F.N. and A.G.; writing—original draft preparation, F.N. and A.G.; writing—review and editing, M.A.C., V.F. and D.K.; visualization, F.N.; supervision, M.A.C., V.F. and D.K.; project administration, M.A.C., V.F. and D.K.; funding acquisition, F.N. and M.A.C. All authors have read and agreed to the published version of the manuscript.

**Funding:** F. Nicoletti’s research contribution is funded by Regione Calabria.

**Institutional Review Board Statement:** Not applicable.

**Informed Consent Statement:** Not applicable.

**Data Availability Statement:** Not applicable.

**Conflicts of Interest:** The authors declare no conflict of interest.

## References

1. Ene, P.C.; Okoh, C.C.; Okoro, P.A.; Egoigwe, S.V.; Chike, K.C. Application of smart DC-Grid for efficient use of solar photovoltaic system in driving separately excited DC motor: Dynamic performance and techno-economic assessments. *Clean. Eng. Technol.* **2021**, *4*, 100136. [[CrossRef](#)]
2. Yang, Y.; Tan, Z.; Jiang, Z.; Yao, J.; Wang, X.; Wang, M.; Xie, Y.; Hu, Z. Influences of uncertainties to the generation feasible region for medium- and long-term electricity transaction. *Glob. Energy Interconnect.* **2020**, *3*, 595–604. [[CrossRef](#)]
3. Zhao, Y.; Song, X.; Wang, F.; Cui, D. Multiobjective optimal dispatch of microgrid based on analytic hierarchy process and quantum particle swarm optimization. *Glob. Energy Interconnect.* **2020**, *3*, 562–570. [[CrossRef](#)]
4. Wurtz, F.; Delinchant, B. “Smart buildings” integrated in “smart grids”: A key challenge for the energy transition by using physical models and optimization with a “human-in-the-loop” approach. *Comptes Rendus. Phys.* **2017**, *18*, 428–444. [[CrossRef](#)]
5. Wan, C.; Zhao, J.; Song, Y.; Xu, Z.; Lin, J.; Hu, Z. Photovoltaic and solar power forecasting for smart grid energy management. *CSEE J. Power Energy Syst.* **2015**, *1*, 38–46. [[CrossRef](#)]
6. Bevilacqua, P.; Perrella, S.; Cirone, D.; Bruno, R.; Arcuri, N. Efficiency Improvement of Photovoltaic Modules via Back Surface Cooling. *Energies* **2021**, *14*, 895. [[CrossRef](#)]
7. Bruno, R.; Bevilacqua, P.; Longo, L.; Arcuri, N. Small Size Single-axis PV Trackers: Control Strategies and System Layout for Energy Optimization. *Energy Procedia* **2015**, *82*, 737–743. [[CrossRef](#)]
8. Nicoletti, F.; Cucumo, M.A.; Ferraro, V.; Kaliakatsos, D.; Settino, J. Performance Analysis of a Double-Sided PV Plant Oriented with Backtracking System. *Math. Model. Eng. Probl.* **2020**, *7*, 325–334. [[CrossRef](#)]
9. Bevilacqua, P.; Bruno, R.; Arcuri, N.; Bevilacqua, P.; Bruno, R.; Arcuri, N. Comparing the performances of different cooling strategies to increase photovoltaic electric performance in different meteorological conditions. *Energy* **2020**, *195*, 116950. [[CrossRef](#)]
10. Ishaque, K.; Salam, Z.; Taheri, H. Simple, fast and accurate two-diode model for photovoltaic modules. *Sol. Energy Mater. Sol. Cells* **2011**, *95*, 586–594. [[CrossRef](#)]
11. Wang, M.; Xu, X.; Yan, Z.; Wang, H. An online optimization method for extracting parameters of multi-parameter PV module model based on adaptive Levenberg-Marquardt algorithm. *Energy Convers. Manag.* **2021**, *245*, 114611. [[CrossRef](#)]
12. Jordehi, A.R. Parameter estimation of solar photovoltaic (PV) cells: A review. *Renew. Sustain. Energy Rev.* **2016**, *61*, 354–371. [[CrossRef](#)]
13. Aoun, N.; Bailek, N. Evaluation of mathematical methods to characterize the electrical parameters of photovoltaic modules. *Energy Convers. Manag.* **2019**, *193*, 25–38. [[CrossRef](#)]
14. Al-Subhi, A.; El-Amin, I.; Mosaad, M.I. Efficient predictive models for characterization of photovoltaic module performance. *Sustain. Energy Technol. Assess.* **2020**, *38*, 100672. [[CrossRef](#)]
15. Saadaoui, D.; Elyaqouti, M.; Assalaou, K.; Ben Hmamou, D.; Lidaighbi, S. Parameters optimization of solar PV cell/module using genetic algorithm based on non-uniform mutation. *Energy Convers. Manag. X* **2021**, *12*, 100129. [[CrossRef](#)]
16. Abbassi, A.; Gammoudi, R.; Ali Dami, M.; Hasnaoui, O.; Jemli, M. An improved single-diode model parameters extraction at different operating conditions with a view to modeling a photovoltaic generator: A comparative study. *Sol. Energy* **2017**, *155*, 478–489. [[CrossRef](#)]

17. Sohani, A.; Sayyaadi, H.; Doranehgard, M.H.; Nizetic, S.; Li, L.K. A method for improving the accuracy of numerical simulations of a photovoltaic panel. *Sustain. Energy Technol. Assess.* **2021**, *47*, 101433. [[CrossRef](#)]
18. Mavromatakis, F.; Kavoussanaki, E.; Vignola, F.; Franghiadakis, Y. Measuring and estimating the temperature of photovoltaic modules. *Sol. Energy* **2014**, *110*, 656–666. [[CrossRef](#)]
19. Faiman, D. Assessing the outdoor operating temperature of photovoltaic modules. *Prog. Photovolt. Res. Appl.* **2008**, *16*, 307–315. [[CrossRef](#)]
20. Mattei, M.; Notton, G.; Cristofari, C.; Muselli, M.; Poggi, P. Calculation of the polycrystalline PV module temperature using a simple method of energy balance. *Renew. Energy* **2006**, *31*, 553–567. [[CrossRef](#)]
21. Abdul, J.; Othman, A.K.; Rigitand, A.R.H.; Saleem, S. Comparison of solar photovoltaic module temperature models. *World Appl. Sci. J.* **2001**, *14*, 1–8.
22. Ceylan, I.; ErKaymaz, O.; Gedik, E.; Gürel, A.E. The prediction of photovoltaic module temperature with artificial neural networks. *Case Stud. Therm. Eng.* **2014**, *3*, 11–20. [[CrossRef](#)]
23. Aly, S.P.; Ahzi, S.; Barth, N.; Abdallah, A. Using energy balance method to study the thermal behavior of PV panels under time-varying field conditions. *Energy Convers. Manag.* **2018**, *175*, 246–262. [[CrossRef](#)]
24. Bevilacqua, P.; Morabito, A.; Bruno, R.; Ferraro, V.; Arcuri, N. Seasonal performances of photovoltaic cooling systems in different weather conditions. *J. Clean. Prod.* **2020**, *272*, 122459. [[CrossRef](#)]
25. Evans, D.L. Simplified method for predicting photovoltaic array output. *Sol. Energy* **1981**, *27*, 555–560. [[CrossRef](#)]
26. Churchill, S.W. A comprehensive correlating equation for laminar, assisting, forced and free convection. *AIChE J.* **1977**, *23*, 10–16. [[CrossRef](#)]
27. Incropera, F.P.; DeWitt, D.P. *Fundamentals of Heat and Mass Transfer*; Wiley: New York, NY, USA, 2002.
28. Sparrow, E.M.; Ramsey, J.W.; Mass, E.A. Effect of Finite Width on Heat Transfer and Fluid Flow about an Inclined Rectangular Plate. *J. Heat Transf.* **1979**, *101*, 199–204. [[CrossRef](#)]
29. Duffie, J.A.; Beckman, W.A. *Solar Engineering of Thermal Processes: Fourth Edition*; John Wiley & Sons: Hoboken, NJ, USA, 2013. [[CrossRef](#)]
30. Bevilacqua, P.; Bruno, R.; Rollo, A.; Ferraro, V. A novel thermal model for PV panels with back surface spray cooling. *Energy* **2022**, *255*, 124401. [[CrossRef](#)]
31. Swinbank, W.C. Long-wave radiation from clear skies. *Q. J. R. Meteorol. Soc.* **1963**, *89*, 339–348. [[CrossRef](#)]
32. Unsworth, M.H.; Monteith, J.L. Long-wave radiation at the ground I. Angular distribution of incoming radiation. *Q. J. R. Meteorol. Soc.* **1975**, *101*, 13–24. [[CrossRef](#)]
33. Ashrae. *Handbook of Fundamentals*; American Society of Heating, Refrigeration, and Air Conditioning Engineers: New York, NY, USA, 1979.